IDA

INSTITUTE FOR DEFENSE ANALYSES

Comparison of Predicted and Measured Multipath Impulse Responses

Kent Haspert
Michael Tuley

May 2010

IDA Document NS D-3957
Log: H 10-000769

This publication is approved for public release and has been accepted by IEEE for publication in a forthcoming issue of *IEEE Transactions on Aerospace and Electronic Systems.*

The Institute for Defense Analyses is a non-profit corporation that operates three federally funded research and development centers to provide objective analyses of national security issues, particularly those requiring scientific and technical expertise, and conduct related research on other national challenges.

About This Publication

This work was conducted under IDA's independent research program (C2136). The views, opinions, and findings should not be construed as representing the official position of the Department of Defense.

Copyright Notice

INSTITUTE FOR DEFENSE ANALYSES

IDA Document NS D-3957

Comparison of Predicted and Measured Multipath Impulse Responses

Kent Haspert
Michael Tuley

This publication is approved for public release and has been accepted by IEEE for publication in a forthcoming issue of *IEEE Transactions on Aerospace and Electronic Systems.*

Comparison of Predicted and Measured Multipath Impulse Responses

Kent Haspert, *Member, IEEE,* and Michael Tuley, *Fellow, IEEE,*

***Abstract*—The fundamental concepts used to evaluate multipath effects date back over 50 years. Today's technology can support wide-bandwidth communications and radar systems that were not available or considered when these multipath concepts were being formulated. This paper presents a slightly modified version of the original analytical approaches for evaluating multipath effects and compares the predicted multipath to data collected from a wideband instrumentation radar. The multipath model presented herein covers both the specular (coherent) and diffuse (noncoherent) components of multipath. The test data were collected for conditions strongly favoring diffuse multipath, but the experimental technique supported detection of any unanticipated specular contributions. Because the purpose of this validation effort was to perform an in-depth examination of multipath effects, the demanding test conditions revealed a couple of real-world effects that had to be addressed. After incorporating these effects into the analytical multipath formulations, we were able to show very close agreement between the predicted and observed multipath.**

I. Introduction

Multipath can degrade radio frequency (RF) transmission by adding unwanted reflected signals to the desired direct-path signal. The unwanted signals are delayed and will consequently have a different phase than the direct-path signal. Depending on the wavelength, geometry, and surface conditions, the total multipath signal can have an amplitude approaching that of the direct-path signal. Moreover, multipath can appear to come from a specular reflection point, or from a diffuse glistening surface, or partly from both. For a stationary transmitter-receiver-reflecting surface geometry, the specular reflection will have a constant phase difference with respect to the direct-path signal. The diffuse reflection consists of a collection of signals of varying amplitudes and phases. The combined multipath returns can therefore add constructively or destructively with the direct-path signal to produce a stronger or weaker (or even vanishing) total received signal. When one or both of the platforms moves, the received signal will fade in and out. This fading can affect RF communications [1], [2], [3] and radar target detection/tracking [4], [5], [6].

In 1953, Ament published a theory for predicting the relative strength of specular reflections assuming a Gaussian random surface [7]. In 1963 Beckmann and Spizzichino published a theory, based in part on their earlier work, for predicting diffuse reflections [8] that also assumed a Gaussian random surface.[1] While considerable empirical evidence over the years tends to support these theories, detailed measurements have been hard to accomplish due to issues such as:

1) Where does one find a Gaussian surface?
2) How does one separately observe the multipath signal in the presence of the direct-path signal?
3) How does one create a sufficiently controlled geometry to support separate measurements of direct and multipath returns over a Gaussian surface?
4) How does one achieve sufficiently high signal-to-noise ratios to directly observe the multipath effects?

This paper develops a model for multipath, based largely on [7], [8], and the work of Barton [9] and then compares the model's predictions to precise multipath measurements. The paper also describes the experimental conditions created to deal with the four questions raised above. The work reported herein concentrates on the diffuse component of the multipath because the diffuse component often receives less attention yet can dominate the multipath signal in many situations. More recent work reported in [10], [11], and [12] addresses multipath and serves as evidence of the ongoing interest in understanding multipath. However, none of these papers provides a direct comparison between their measured data and multipath models such as the one presented herein.

II. Multipath Model

For air-to-air communications, Figure 1 shows a direct path between the transmitter and the receiver and several other paths between the transmitter and the receiver that involve scattering of RF signals off the earth's surface.[2] The propagation paths involving scattering are longer than the direct path. The path from the transmitter to the specular point (point S in the figure) and then from the specular point to the receiver defines the minimum multipath path length. However, scattering can also occur from points on either side of the specular point (i.e., those points labeled D in the figure), and these multipath paths have a longer total path length.

Institute for Defense Analyses, 4850 Mark Center Dr, Alexandria, VA 22311.

Manuscript received ; revised .

[1]The assumption of a Gaussian random surface might seem simplistic and unwarranted in many cases. However, it seems reasonable, useful, and appropriate in many real-world situations such as the following: RF propagation to/from a moving platform when even a non-Gaussian surface would, upon repeated sampling as the platform moves and the geometry changes, appear to behave statistically like an approximately Gaussian surface (i.e., due to the central limit theorem); RF propagation to/from a stationary platform above the ocean surface, where wave motion randomizes the reflecting surface.

[2]Due to reciprocity, the locations of the transmitter and receiver can be interchanged without affecting the theory.

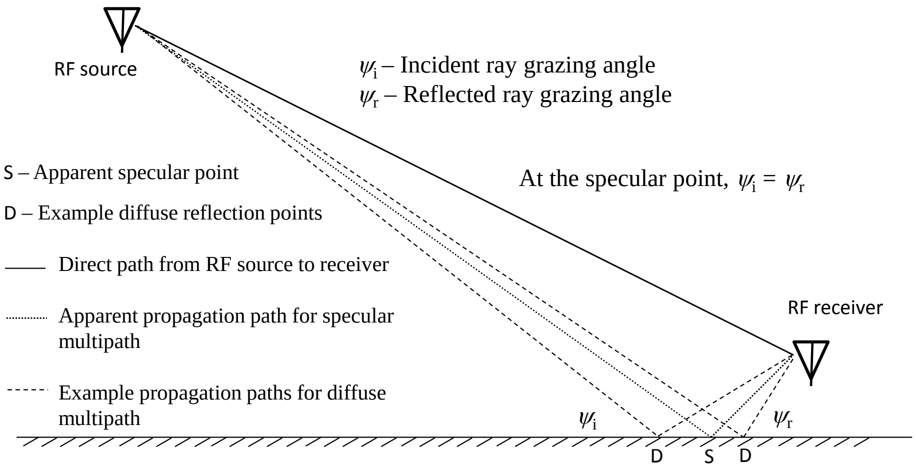

Fig. 1: Multipath paths

A. *Specular and Diffuse Multipath*

Smooth, mirror-like surfaces produce specular multipath. Although the specular multipath appears to come from a single point, it actually involves coherent integration over a wide portion of the surface. Rough surfaces produce diffuse multipath. In this case, the reflected RF signals over the surface add noncoherently and typically appear weaker than specular multipath. However, diffuse multipath appears to come from a sizable region, known as a glistening surface [8], [9], and it is spread in path delay. While the peak amplitude of the diffuse multipath may sometimes be relatively weak, the total strength of the diffuse multipath can become significant after noncoherently combining the energy coming from a large glistening surface.

Ament's formula (1) predicts the specular reflection coefficient (i.e., the voltage ratio of the scattered to incident RF, assuming a perfectly reflecting surface) as a function of the rms surface height variation (σ_h), the grazing angle (ψ), and the wavelength (λ):

$$\rho_s = \exp\left[-2\left(\frac{2\pi\sigma_h \sin(\psi)}{\lambda}\right)^2\right] \tag{1}$$

In subsequent work [13], Miller et al. developed the following modification to Ament's formula:

$$Ps = 2\left(\frac{2\pi\sigma_h \sin(\psi)}{\lambda}\right)^2 \tag{2}$$

$$\rho_s = \exp\left[-Ps\right] I_0\left(Ps\right) \tag{3}$$

where Ps from (2) is the parameter inside the bracket in (1) and I_0 represents the modified Bessel function of zero order. In [14], Beard provides measured data that corroborates the formulation in [13].

Figure 2 plots both Ament's formula (1), shown as the thinner lines, and the modified formula (3). It shows that the two formulas begin to diverge when (ρ_s) falls below about 0.5. The figure illustrates the variation in the specular reflection coefficient as a function of the grazing angle for several ratios of rms surface height to wavelength. For a representative L-band RF source (λ = 0.3 m) on a platform at 1500 m, a receiver at 30 m, a ground range of 75 km, and for σ_h = 0.30 m, then ρ_s = 0.97. See Case 1 on the graph. Case 2 assumes the same geometry but an X-band RF source (λ = 0.03 m), and in this case ρ_s = 0.23. Assuming that all the RF energy striking the surface either goes into specular or diffuse multipath, then by conservation of energy as suggested by [15], the corresponding diffuse reflection coefficient can be inferred to be given by $\rho_d = \sqrt{1-\rho_s^2}$. For the two assumed cases, this results in ρ_d = 0.25 and 0.97, respectively.

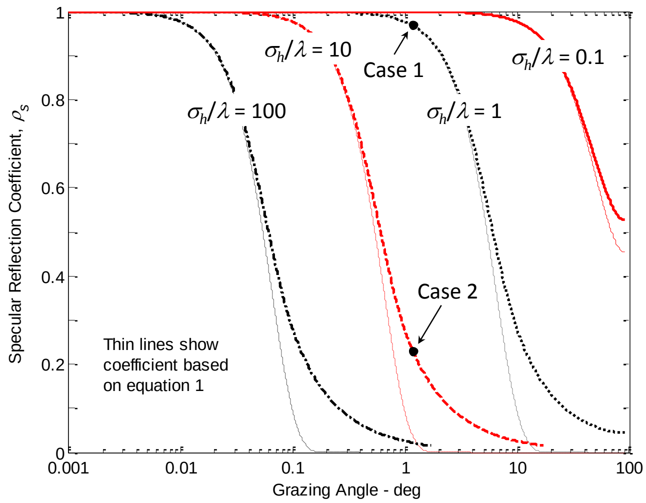

Fig. 2: Specular Reflection Coefficient

While the geometry discussed in subsequent sections of this paper is not affected by a divergence factor, the specular reflection coefficient just presented (3) should be multiplied by a spherical-earth divergence factor (i.e., ρ_s' = ρ_s D). From [16], the following equation calculates the divergence factor:

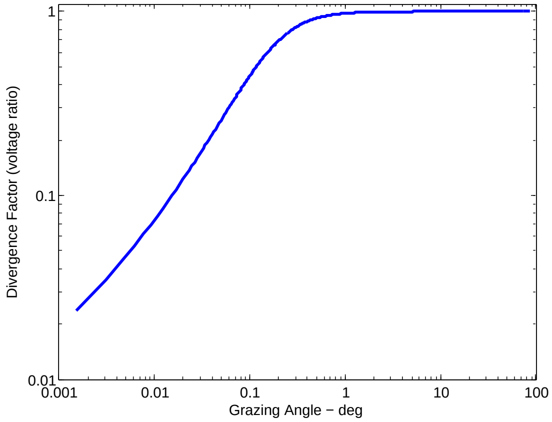

Fig. 3: Divergence Factor

$$D = \left(1 + \frac{2G_1G_2}{R_e(G_1+G_2)\sin\psi}\right)^{-1/2} \tag{4}$$

where G_1 and G_2 represent the ground range from the specular point to the transmitter and receiver, R_e represents the effective (e.g., 4/3) earth radius, and ψ represents the grazing angle. Figure 3 shows the variation of the divergence factor as a function of the grazing angle. As examples, grazing angles of 1^0 and 0.5^0 give divergence factors of 0.98 and 0.92, respectively.

B. *Impulse-Response Curve for Specular Multipath*

Because the specular return appears as if it comes from the specular point, the multipath path delay is given by the path-length difference between the direct path and the specular path. However, the *intensity* of the specular return is a function of the specular reflection coefficient, ρ_s, and three other factors:

1) $\sqrt{G_{ant}}$, where G_{ant} is the power ratio of the radar antenna gain in the direction of the specular point to the antenna gain along the direct path to the target.
2) Γ_v, the Fresnel reflection coefficient that considers the surface conductivity and dielectric constant and determines how much of the incident radar signal is absorbed by the surface, where the subscript denotes the radar's polarization (where *v* indicates vertical, which applies in the case analyzed herein).
3) ρ_{veg}, a vegetation factor that determines how much the vegetation on the surface attenuates the reflected signal.

Equation 5 expresses the strength of the specular return relative to the strength of the direct-path return as a function of these four factors:

$$\text{Specular/Direct path voltage} = \rho_s\sqrt{G_{ant}}|\Gamma_\nu|\rho_{veg}. \tag{5}$$

These factors combine to produce a simple specular impulse response curve (IRC) of voltage impulses, as shown in Figure 4. In this figure, the specular impulse appears delayed with respect to the direct-path impulse. The amount of range delay is given by the following formula:

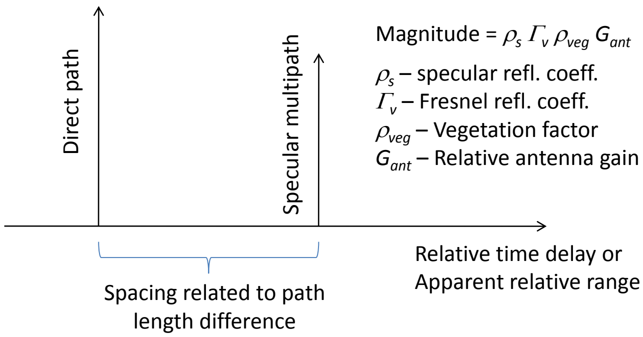

Fig. 4: Specular impulse response curve

$$\text{Specular range delay} = R_1 + R_2 - R, \tag{6}$$

where R_1 is the distance from the transmitter to the specular point, R_2 is the distance from the specular point to the receiver, and R is the direct-path distance between the transmitter and the receiver.

C. *Glistening Surface and Diffuse Multipath*

A rough surface produces scattering, but the surface roughness makes the phase relationships among the reflections across the surface unpredictable (or at least infeasible to address in anything other than a statistical sense). In [9], Barton extended the rough surface formulation of Beckmann and Spizzichino [8]. These sources provide the basis for formulating a single equation that describes the diffuse multipath return from an arbitrary small patch of area *dA* lying somewhere on the glistening surface. The last term in the following equation differs from the one provided in [9] to incorporate what the authors feel provides a more realistic representation of surface shadowing that can occur at low grazing angles and thereby reduce the effective area for accumulating multipath diffuse energy, as described below.

$$\frac{\text{Diffuse voltage from } dA}{\text{Direct path voltage}} = \sqrt{\frac{1}{4\pi}\left(\frac{R}{R_1R_2}\right)^2 \frac{1}{\beta_0^2}\exp\left(-\frac{\beta^2}{\beta_0^2}\right)dA} \cdot |\Gamma_v| \cdot \rho_{veg} \cdot \sqrt{G_{ant}} \cdot \rho_{roughness}\sqrt{S_f} \tag{7}$$

where:

$\frac{1}{4\pi}\left(\frac{R}{R_1R_2}\right)^2$ – the one-way spreading loss

$\frac{1}{\beta_0^2}\exp\left(-\frac{\beta^2}{\beta_0^2}\right)$ – expected bistatic radar cross section per unit area (σ_0) of the diffuse patch defined by dA, where β_0 is the mean square value of the surface slope over the region of interest [17] and β is the angle between the bisector of the R_1 and R_2 rays and the local vertical.[3]

[3]As shown in [18], the "region of interest" is governed by the extent of the first Fresnel zone. Over water this typically exceeds the surface correlation distance, but over land this may not always be true.

$\rho_{roughness}$ – roughness factor (potential maximum diffuse return multiplier)
$\sqrt{S_f}$ - a shadowing factor (probability that dA is actually seen by both the transmitter and receiver)

The Fresnel reflection coefficient in (7) incorporates the surface dielectric constant, ϵ_r, the surface conductivity, σ_e, the wavelength,λ, and the grazing angle at the specular point, ψ. As shown in [9], the following equations yield the value of Γ_v (or Γ_h):

$$\epsilon_c = \epsilon_r - j60\lambda\sigma_e \quad (8)$$

$$\Gamma_p = \frac{\epsilon_c^{\bar{p}} \sin\psi - \sqrt{\epsilon_c - \cos^2\psi}}{\epsilon_c^{\bar{p}} \sin\psi + \sqrt{\epsilon_c - \cos^2\psi}} \quad (9)$$

where $p = h$, $\bar{p} = 0$ for horizontal polarization, and $p = v$, $\bar{p} = 1$ for vertical polarization.

The antenna factor term in (7) is different from the specular antenna factor in that it varies over the glistening surface, as for that matter do most of the other terms in this equation. The spreading-loss term contains the direct-path range to the receiver (R), the range from the transmitter to the differential patch (R_1), and the range from the differential patch to the receiver (R_2). The above equation has an exponential term where the argument of the exponent is the ratio of the squares of β and β_0, where β is the surface tilt required at the patch to support a specular reflection of RF energy off the patch that will strike the receiver. The exponential term has the form of a Gaussian probability distribution. Near the specular point, the required value of β is nearly zero, so the expected σ_0 is largest for patches near the specular point. For points further away from the specular point, the required surface slope to support multipath reflections becomes greater, so the expected value of σ_0 falls off for patches further from the specular point.[4] The practical extent of the glistening surface is typically treated as the locus of points where $\beta/\beta_0 = \sqrt{2}$ (i.e., the 2-sigma boundary of a Gaussian having a similar exponential term) or perhaps $\beta/\beta_0 = \sqrt{4.5}$ (i.e., the 3-sigma boundary). Figure 5 depicts both the 2- and 3-sigma glistening surface boundaries for an RF source at 1,000 m height and a receiver at 250 m height that is 10 km downrange, assuming $\beta_0 = 0.05$ rad. The figure also assumes a flat earth and the appendix gives the formulation used to generate these contours.[5] At longer ranges, one often assumes 4/3 earth curvature to allow for refraction and maps the curved earth onto a flat plane as described in [16]. The extent of the glistening surface appears similar to an ellipse for this example, but the actual shape is more complicated mathematically. In the analyses reported herein, the dA term in the above formula consisted of narrow cross-range strips. Multiple strips were used to cover the entire downrange extent of the glistening surface. When considering moving platforms, however, one often would like to obtain a two-dimensional range-Doppler IRC. In this case, the individual dA cells need to be relatively small in both the downrange and cross-range dimensions over the glistening surface. Essentially all the diffuse multipath energy is found by integrating (7) over the 2- or 3-sigma extent of the glistening surface.

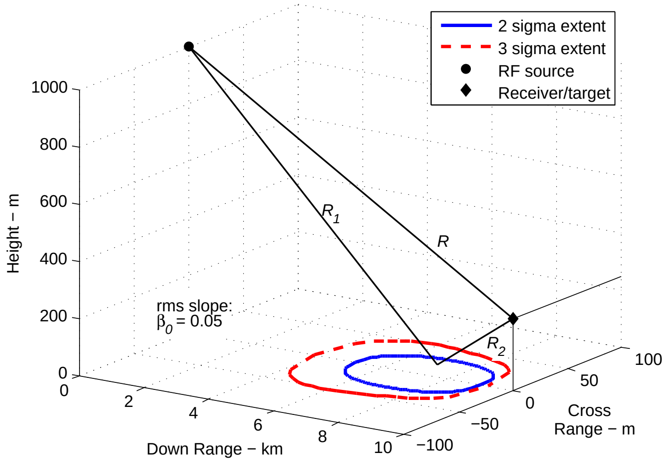

Fig. 5: Extent of the glistening surface

While the practical extent of the glistening surface considers only the exponential term, the strength of the diffuse return also varies considerably due to the effect of the spreading-loss term. In fact, for points on the glistening surface closer to the receiving point, the term R_2 becomes small, and the overall intensity of diffuse multipath from that differential patch becomes relatively large. The roughness factor in (7) represents application of the specular reflection coefficient formula at the location of the differential patch, as developed by Barton [9] and given by $\rho_{\text{roughness}} = \sqrt[4]{(1-\rho_s(\psi_1)^2)\cdot(1-\rho_s(\psi_2)^2)}$, where ψ_1 and ψ_2 represent the incident and reflected grazing angles associated with each dA patch. The shadowing factor in (7) is calculated via the following equations:

$$L_i = \frac{\beta_0 \cdot \exp\left[-\left(\frac{\tan\psi_i}{\beta_0}\right)^2\right]}{\sqrt{\pi}\cdot\tan\psi_i} - \text{erfc}\left(\frac{\tan\psi_i}{\beta_0}\right) \quad (10)$$

$$S_{f_i} = \left[1 - \frac{1}{2}\text{erfc}\left(\frac{\tan\psi_i}{\beta_0}\right)\right] \Big/ (L_i + 1) \quad (11)$$

where erfc() is the error function complement. The value of S_f is given by multiplying the values computed from the point of view of the transmitter and the receiver, that is, $S_f = S_{f_1} \cdot S_{f_2}$. These two equations represent an alternative, but equivalent, statement of equations (21) and (24) in a paper provided by Smith [19].

D. *Impulse-Response Curve for Diffuse Multipath*

The diffuse multipath model treats the phase relationships among the returns over the glistening surface as unpredictable random quantities and merely adds the powers of the returns from the various differential patches (i.e., noncoherent integration). The various differential patches have different

[4]The fact that the diffuse multipath tends to be strong in the same region where the specular multipath occurs makes separately observing the specular and diffuse components of multipath rather difficult. As will be shown shortly, we chose to create test conditions where we expected minimal specular multipath so as to allow direct observation of the diffuse multipath.

[5]The formula for the extent of the glistening surface in [8] represents an approximation while the formulation in the appendix is exact, and we believe not previously reported.

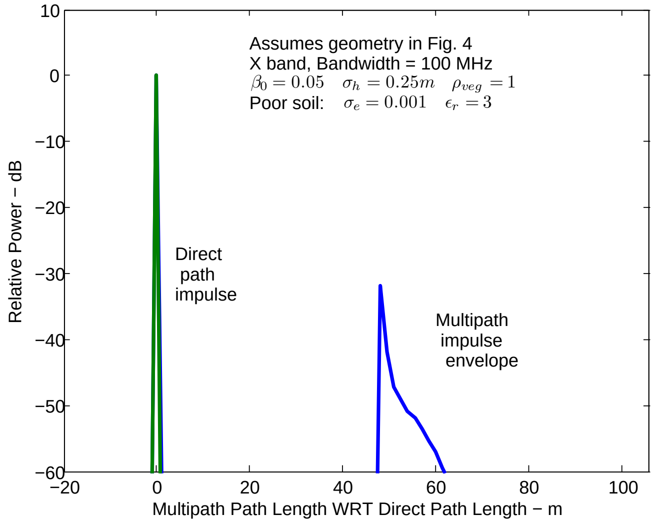

Fig. 6: Example diffuse impulse-response curve

path delays, however, and an RF source consisting of a wide-band radar can typically resolve these delays over the glistening surface. Figure 6 shows a one-way IRC for the diffuse multipath. The first portion of the diffuse-return IRC combines the energies associated with those portions of the glistening surface that have a path delay within one radar range-resolution bin of the specular path delay. Additional portions of the glistening surface have longer path delays, and they produce a one-way diffuse IRC that appears to form a series of diminishing impulses. Although the strength of the diffuse return from a patch increases as one nears the target, the total number of patches falling within a given range bin decreases rapidly, so the net effect produces diminishing impulses for the regions of the glistening surface that have greater range delays. The roughness in the curve is due to the assumed bandwidth and the resulting pairing of dA strips with the path-delay bins.

E. *Total Multipath Impulse-Response Curve*

The total IRC consists of noncoherent addition of the specular and diffuse multipath contributions from curves such as Figures 4 and 6. The direct-path return appears in both Figures 4 and 6 to provide a timing/path delay reference for the multipath returns. It should not be added twice when forming the total multipath IRCs. For many geometries and surface conditions, the diffuse multipath energy exceeds the specular multipath energy. It also turns out that diffuse multipath produces a more complicated effect than the specular multipath because of its range/time extent and the random phases associated with each of the individual diffuse IRC impulses. Further, for monostatic radar applications the effective IRC essentially consists of a convolution of the one-way IRC with itself.

III. Validation Testing

The foregoing specular and diffuse multipath formulations support the generation of IRCs that characterize multipath as a function of the encounter geometry and the observed or estimated surface conditions. These equations provide a tidy analytical formulation for predicting multipath effects and characterizing these effects via IRCs. However, the original multipath formulations of [8] and [9] that underlie the methodology did not explicitly consider their applicability to wide-bandwidth systems. Therefore, the authors recognized the need to validate the foregoing theoretical formulations in the context of wide-band RF systems. The most direct way to do this appeared to entail the use of a wide-band instrumentation radar observing a point scatterer (e.g., a calibration sphere), with a relatively rough surface between the radar and the point scatterer, and then directly observing the diffuse multipath IRC. However, our experimental configuration differed from [11] in that it utilized a dual-antenna, wide-band radar to obtain fine resolution in the downrange structure of the diffuse multipath. The rough surface minimized the specular portion of the multipath.

A. *Atlantic Test Range Experimental Configuration*

The Atlantic Test Range experiments used two nominally identical high-gain X-band radar antennas sitting near the coastline of the Chesapeake Bay and a tethered sphere a few miles off shore. One of the antennas tracked a tethered sphere and bounced RF energy off it. The other antenna pointed downward and observed the glistening surface. The downward-looking antenna only received radar signals but had its local oscillator synchronized with the upward-looking antenna. Figure 7 illustrates the test configuration. This experimental configuration provided direct observation of the one-way multipath path. Because the calibration sphere appears as a point scatterer, the experiment directly measured the one-way IRC. The relatively short ranges and low grazing angles generate an IRC with relatively little range delay, which necessitated the use of a wide-bandwidth radar to resolve the structure of the IRC.

During the test, the winds varied between 20 and 30 kts out of the north. This created approximately 3.5 ft waves with a period of about 3 seconds. The high-gain, approximately 10 ft diameter radar antennas have a 3 dB beamwidth of about 2/3 of a degree, as shown by the measured antenna patterns in Figure 8. The upward-looking transmitting and receiving antenna, designated X1, tracked the tethered sphere as the winds blew it around. The sphere's height varied from about 310 to 475 ft and the range varied from about 13,900 to 14,200 ft. The downward-looking, receive-only antenna, designated X2, stepped through 21 look-down angles between $4°$ and $0°$ to scan the glistening surface. The downward-looking antenna recorded data for about 30 seconds at each look-down step and ran through this range of look-down angles twice. The test conditions produced σ_h of about 27 cm and β_0 of 0.055 radians [20], which yielded an expected ρ_s of 0.179 (or 0.005 if only applying Ament's formula). The radar transmitter employed 256 4-MHz steps to cover 9.5 to 10.52 GHz. This produced an inherent range resolution of 14.64 cm, but through 2:1 oversampling, the effective range-bin size became 7.32 cm. The radar transmitted a 1.5 μs pulse every 40

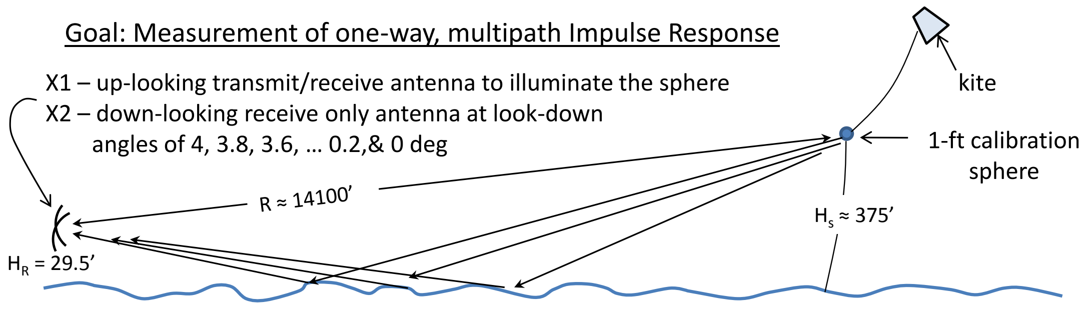

Fig. 7: Atlantic Test Range test configuration

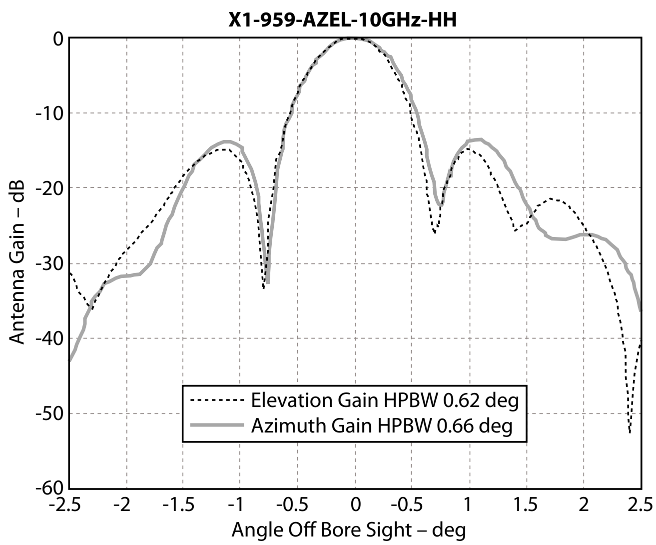

Fig. 8: Measured antenna patterns

μs. Hence, an individual return was formed every 10.24 msec. Upon completion of the test, both the X1 and X2 radars tracked a free-flying calibration sphere to provide range and amplitude calibrations for both radar channels.

B. *Data-Analysis Procedures*

The test conditions suggest that the diffuse multipath should totally dominate the specular multipath.[6] However, we wanted to validate this theoretical prediction by analyzing the data in such a way that any specular multipath significantly above the predicted value would become readily apparent. Also, the diffuse multipath model assumes a statistically random Gaussian surface. During the course of any individual return formed over a 10.24 ms interval, the sea surface would appear essentially stationary and not necessarily Gaussian. Over the course of the surface's approximately 3-second wave period, however, the diffuse glistening surface should appear random, in accordance with the assumption inherent in the diffuse multipath formulation. The desire to see any significant specular return (if it were to exist) and the desire to create a random glistening surface matching the one assumed in the diffuse return model both suggested the use of long (i.e., greater than 3 sec.[7]) coherent processing intervals (CPIs). If the specular return were to be substantially stronger than predicted, then the long CPIs would allow it to be readily observed after proper motion compensation. The use of long CPIs also provided the added benefit of enhancing the observed signal-to-noise ratio (SNR).

To achieve these long CPIs, we needed highly accurate motion compensation of the sphere's position. William Leeper, a system engineer associated with the Atlantic Test Range, provided software to achieve the desired motion compensation. The X1 (transmit/receive) antenna gave the apparent position of the sphere within the limits of the radar's range gate as shown in the left-hand portion of Figure 9. The motion compensation involved measurement of the phase of the direct-path return associated with each of the individual frequency steps. The individual phase measurements were converted into actual range measurements and then fed into a second-order motion model to generate finely resolved target positions versus time. This refined target position history was then converted into phase corrections for each frequency step. After applying these phase corrections to the measured data, the apparent target position appeared stationary within the radar's range gate, as shown in the right-hand portion of Figure 9 over the entire approximately 30 sec. of an antenna look-down-angle step.

The position compensation shown for the direct path should also keep the specular path length focused, assuming the relative multipath geometry remains essentially constant. If the relative path-length difference varies by less than 0.075λ (or 2.25 mm at X-band), then the instantaneous specular returns from each 10.24 ms return should add coherently within about 1 dB. Figure 10 shows the relative path-length difference over an example X2 antenna look-down angle data-collection period and shows those intervals greater than 3 seconds where the path-length difference meets this $\pm$2.25 mm criterion. We then processed long CPIs for each of these "constant" path-length-difference intervals.

[6]With $\rho_s = 0.1787$, the specular power is related to the square of this value, or about 3% of the diffuse power.

[7]A 3-second CPI meant the coherent integration of at least 300 individual 10.24 ms measurements.

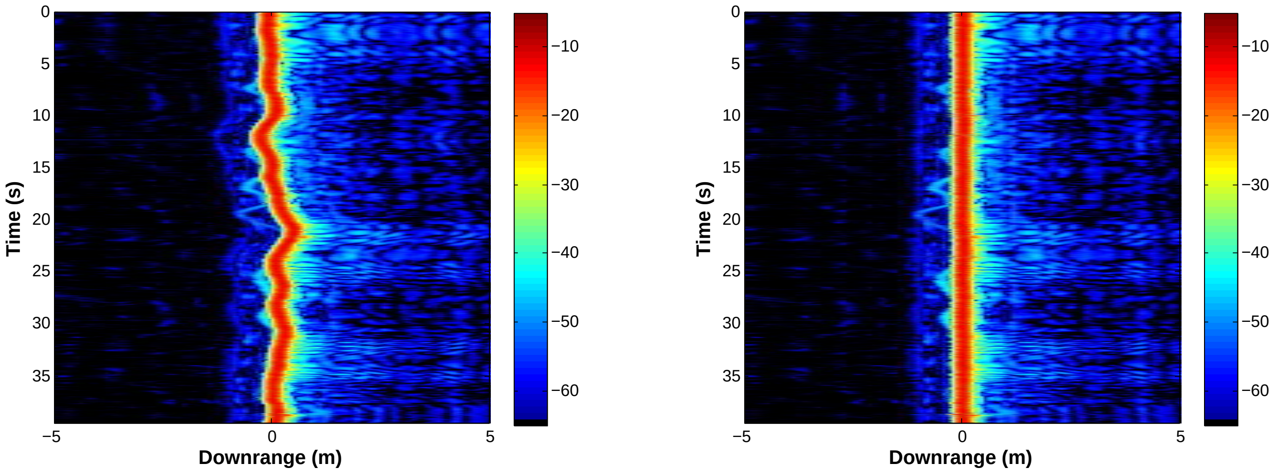

(a) Direct path return before focusing

(b) Direct path return after focusing

Fig. 9: Direct-path position compensation for sphere.

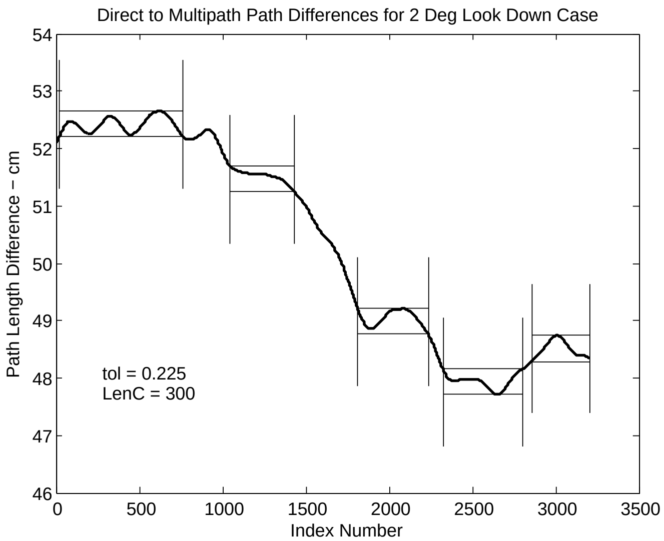

Fig. 10: Relative path lengths for the sphere

C. Initial Comparison of Predicted and Measured Impulse-Response Curves

We used the formulations for the specular and diffuse multipath, along with the specific test conditions (e.g., σ_h, β_0, sphere range and altitude, and assessment of the X2 antenna gain across the glistening surface for the look-down angle) to generate a predicted IRC. Figure 11 shows the predicted location and intensity of the total predicted multipath, the specular-only portion of the multipath, and the anticipated direct path entering into the side-lobe of the downward-looking X2 antenna for the longest intervals identified in Figure 10. The figure also shows an overlay of the measured return seen in the X2 antenna for the same "constant" geometry evaluation interval. In Figure 11, and all of the subsequent IRC plots, the vertical axis shows the return seen by the X2 antenna, but the IRC values are plotted in dB relative to the direct path return power seen by the X1 (upward looking) antenna. The horizontal axis shows the radar-perceived relative ranges in meters (which correspond to one-half the one-way relative path lengths).

At this point, the comparison between the predicted and measured IRCs looks poor. At least the predicted peak value for the multipath roughly agrees with the measured peak value,[8] but the measured return spreads across more range bins and has a slower decaying tail than the predicted values. This IRC-breadth discrepancy appeared in all cases we examined. The measured return also shows energy arriving *before* the direct-path return into the X2 antenna sidelobe. Even though this early return is below –60 dB, it is above the approximately –70 dB noise floor and consistently appeared in every case. We will next provide further analyses of these two discrepancies.

D. Effect of the Radar's System Response Function

The *observed* radar return from a sphere is a function of the radar electronics (e.g., any band-pass filters), wave-guide reflections, and any post processing of the measured I and Q data associated with forming the radar's return (e.g., weighting functions associated with the FFTs). During our tests, the X1 transmit/receive antenna was directly observing the sphere. Note that the measured/processed return from the sphere spreads across several range-resolution bins, as shown by the inset in the upper portion of Figure 12. Because the X1 and X2 radars were essentially identical (and any post-processing was clearly identical), we used the observed X1 sphere-response curve as a representation of the X2 system-response function. After convolution of the predicted multipath IRC with the observed X1 system-response curve, we obtained a modified predicted IRC that agrees much better with the majority of the measured IRC, as shown in the lower panel of

[8] The peak of the multipath portion of the IRC is about 10 dB less than that shown in Fig. 6 as a consequence of the test geometry, the antenna patterns, and the electrical properties of the surface.

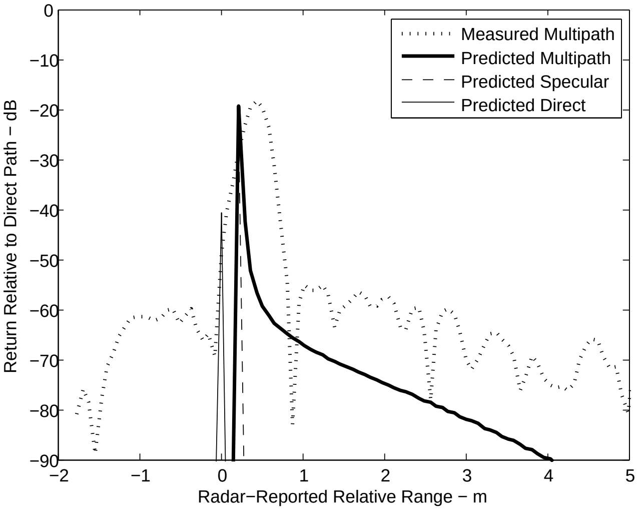

Fig. 11: Initial IRC comparison

Figure 12. However, the early portion of the measured return remains and this required further investigation.

E. Explanation of the Early Portion of the Measured Return

The ATR's Cassegrain antenna appears responsible for the early return seen in the measured data. The left-hand panel in Figure 13 illustrates a possible way that direct-path energy could seem to arrive earlier than expected. Instead of all the off-bore-sight direct-path return seen by the X2 antenna bouncing off the main reflector, we believe that a portion of the off-bore-sight direct-path return diffracted around the sub-reflector and directly entered the antenna feed horn. Because this path is shorter than the nominal path involving the main reflector by about 1.7 m, any such diffracted response would appear to arrive early by about 2.83 nsec (or about 0.85 m in radar-perceived range).

This low-level, early arriving, diffraction-induced affect is usually never seen, but in our case, we have a high-range-resolution system that also produces peak SNR levels of about 70 dB. A back-of-the envelope calculation showed that the diffraction around the sub-reflector could be as large as about 40 dB below the incident off-bore-sight signal, assuming perfect knife-edge diffraction. Because the sub-reflector has a rolled edge that would further reduce the diffraction, we chose to set the diffraction level at 58 dB below the incident off-bore-sight direct-path signal. The right-hand panel in Figure 13 shows a modified theoretical IRC (before convolution with the system response curve) that includes an early impulse at a negative range of 1.7/2 = 0.85 m to represent this hypothesized diffraction affect.

F. Composite Comparison of Multiple Impulse Response Curves

We calculated theoretical IRCs for each of the look-down angles between 4 and 1 degrees for each of the "constant" relative path-length geometries, convolved these geometries with the observed X1 antenna system response curve, and

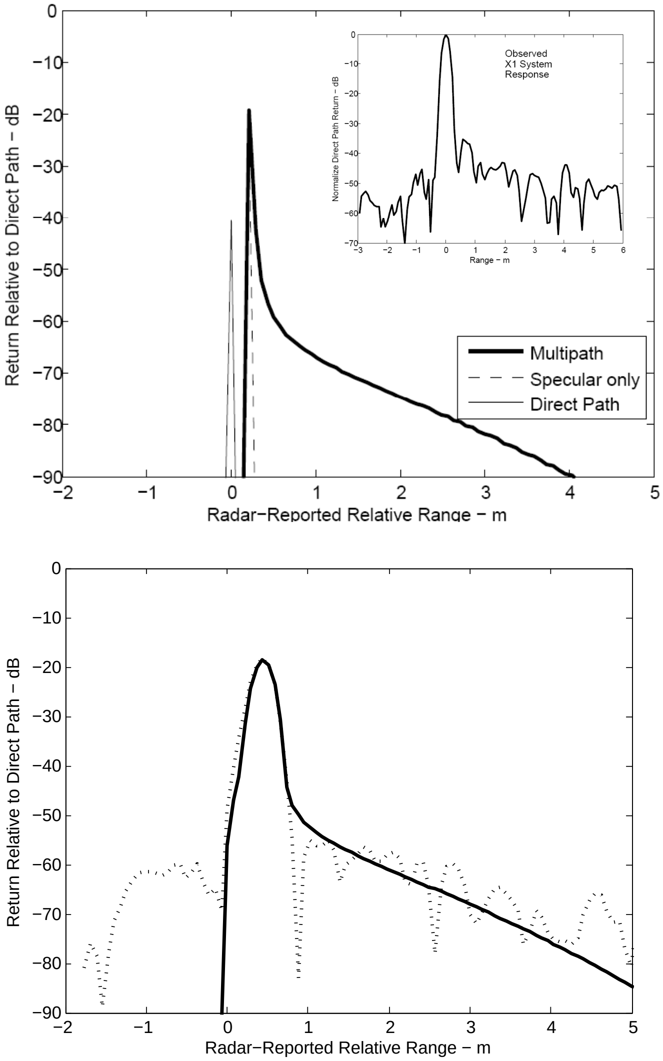

Fig. 12: Revised IRC after convolution with observed X1 system response

compared these theoretical returns with the measured data. Figure 14 shows these comparisons at sample look-down angles of 3°, 2°, and 1°.

The theoretical IRC represents an expected-value return, so we wanted to combine all the measured data for the cases analyzed to get as good an estimate of the mean measured return as possible.[9] Therefore, we noncoherently combined the four cases shown above and all the other measured and predicted returns with CPIs greater than 3 sec. to form a summary plot of all of the data. The non-coherent summations of these IRCs were weighted by the length of the CPI. Figure 15 shows a comparison between the combined theoretical and measured IRCs. The curves agree within about 1.5 dB for the positive-range portions of the IRCs. Although the theoretical

[9]Because the individual "constant" geometry look-down angle measurement cases do not reveal any unanticipated levels of specular multipath (i.e., no excessively strong return in the first range bin of the measured multipath), we decided to noncoherently combine individual "constant" geometry returns such as the four examples shown in Figure 15 to develop a better measurement of the mean multipath return in each range bin.

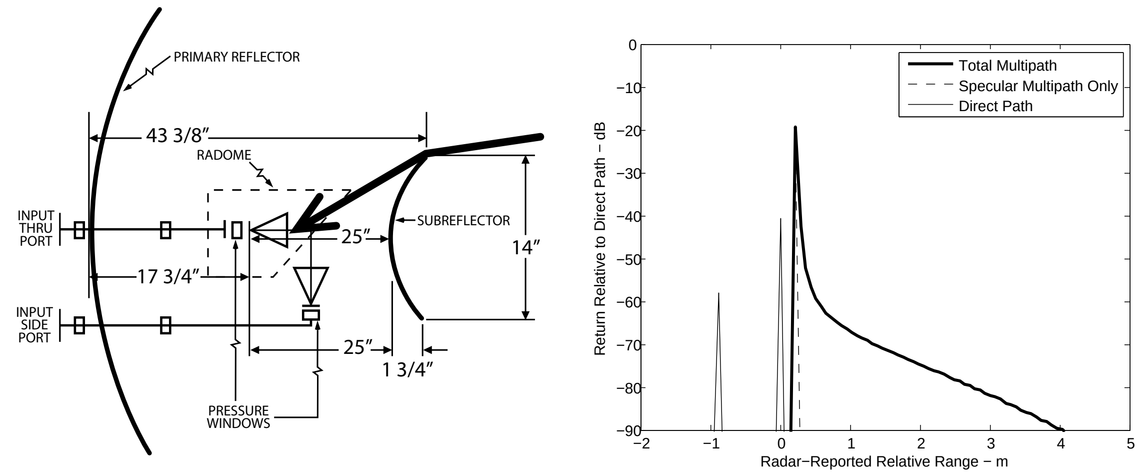

Fig. 13: Cassegrain antenna geometry and its effect on initial IRC prediction

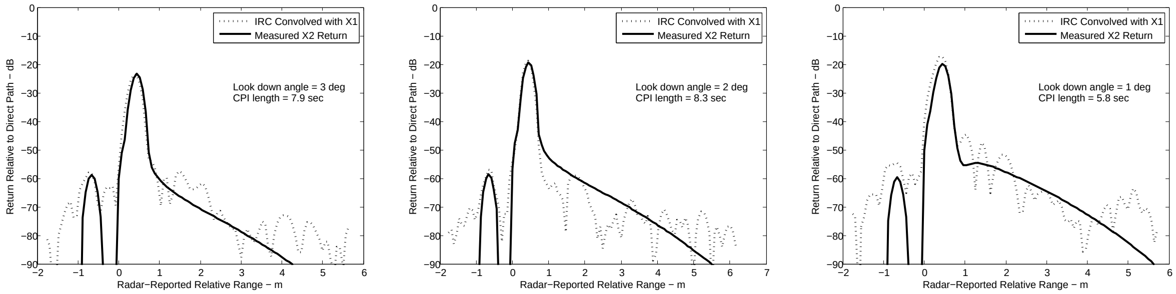

Fig. 14: Three example comparisons between the theoretical and measured IRCs

multipath formulation incorporates a number of parameters, we achieved the high level of agreement shown in Figure 15 without adjusting any of the parameters in (7) to enhance the level of agreement. Also, while Figure 15 shows some discrepancy between the measured and predicted breadth of the early arriving energy, we have only attempted to provide a plausible explanation for the early arriving portion of the measured return, which Figure 15 appears to give. Because of some controversy regarding whether (1) or (3) is more appropriate, we provide Figure 16, which shows that (3) provides about a 1.5 dB improvement in the peak response. Also, the difference between the measured and computed curves in the region between 0 and 0.2 meters in Fig. 16 may well be due to an underestimate of the direct path return entering the side lobe of the X2 antenna. Unfortunately, we did not have the time or resources to calibrate the X2 antenna pattern and used instead the X1 antenna pattern shown in Fig. 8. Moreover, the X1 antenna pattern was only measured out to 2.5 degrees and for some X2 look-down angles the the side-lobe angle for the direct path exceeded this value.

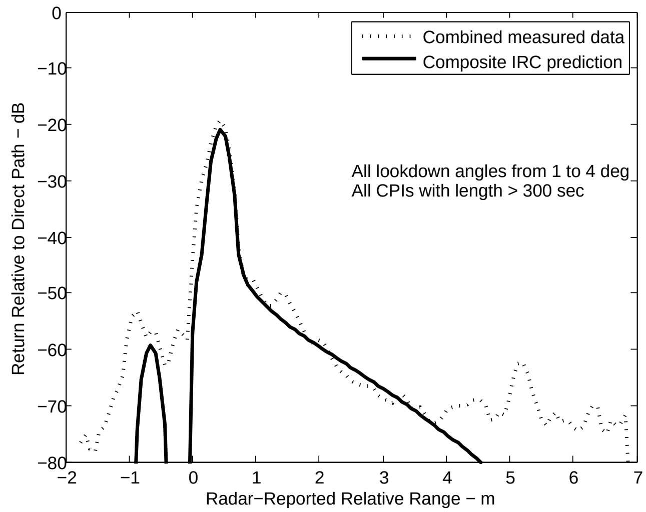

Fig. 15: Combined theoretical and observed IRCs

IV. Summary and Conclusions

The reported comparisons between the observed and measured IRCs appear to provide strong support for the validity of the multipath formulations presented herein once one accounts for the inherent system response. We were especially interested in validating the diffuse multipath theory for wide-bandwidth applications, and the test conditions and results appear to validate that portion of the multipath model. In these tests, we unexpectedly observed an early arriving signal in the measured data. Although we did not investigate the physics of the early arriving signal in detail, we believe that the diffraction argument presented herein provides a plausible explanation for this effect. The results also indicate that the theoretical IRC

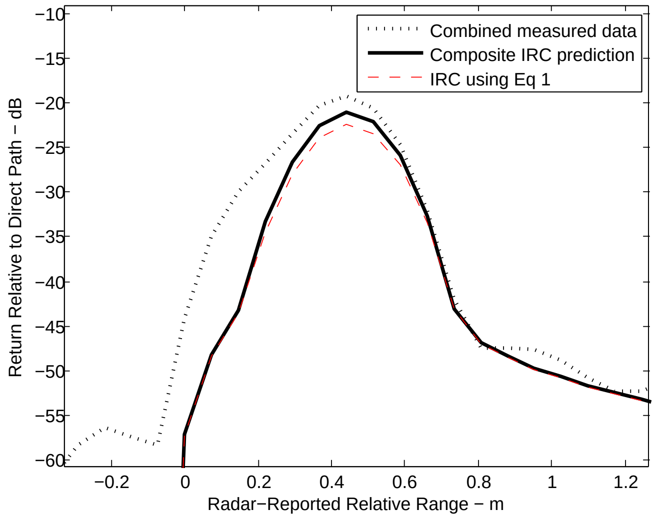

Fig. 16: Effect of Alternative Specular Formulations

formulation should not be used without considering the overall system response characteristics of the radar. The discrepancy in the early portion of the multipath prediction is most likely due to an imperfect representation of the X2 antenna side lobes. During these tests, the sphere moved relatively slowly so we did not look at any Doppler spreading of the returns. However, additional tests from a moving impulse-generating repeater would represent one way to validate any Doppler spreading that the theoretical multipath model might predict.

APPENDIX
CALCULATION OF EXTENT OF GLISTENING SURFACE

The extent of the glistening surface is defined as the location on the surface where the local slope is some multiple of the RMS slope, β_0. Figure A-1 shows the geometry assumed throughout this Appendix. Because the equation for the strength of the diffuse multipath contains the exponential $\exp(-\beta^2/\beta_0^2)$, which has the form of the exponential in a Gaussian distribution if one lets $\beta_0^2 = 2\sigma^2$, then the two- and three-sigma edges are defined by $\beta = 2\sigma$ (hence $\beta = \sqrt{2}\beta_0$) and by $\beta = 3\sigma$ (hence $\beta = \sqrt{4.5}\beta_0$). Therefore, in general the limiting value of β (i.e., β_{lim}) at the edge of the glistening surface is given by

$$\beta_{lim} = k\beta_0/\sqrt{2}, \tag{A-1}$$

where k is number of standard deviations.

We will calculate the glistening surface assuming a flat earth and begin by defining unit vectors $\mathbf{U}_1$ and $\mathbf{U}_2$ as follows:

$$\mathbf{U}_1 = \left(-x\mathbf{i} + H_r\mathbf{j} - z\mathbf{k}\right)/R_1 \tag{A-2}$$

where $R_1 = \sqrt{x^2 + H_r^2 + z^2}$ and

$$\mathbf{U}_2 = \left((G-x)\mathbf{i} + H_t\mathbf{j} - z\mathbf{k}\right)/R_2 \tag{A-3}$$

where $R_2 = \sqrt{(G-x)^2 + H_t^2 + z^2}$

A unit vector that bisects $\mathbf{U}_1$ and $\mathbf{U}_2$ is $\mathbf{U}_B = (\mathbf{U}_1 + \mathbf{U}_2)/|\mathbf{U}_1 + \mathbf{U}_2|$ and the local slope that allows rays to bounce between the radar and the target is $\beta = \cos^{-1}(\mathbf{U}_B \bullet \mathbf{j})$, hence upon setting $\beta = \beta_{lim}$ at the boundary of the glistening surface we obtain the following:

$$\begin{aligned} C_B &= \cos(\beta_{\text{lim}}) = \cos\left(\frac{k\beta_0}{\sqrt{2}}\right) \\ &= \frac{H_r/R_1 + H_t/R_2}{\sqrt{\left(\frac{-x}{R_1} + \frac{G-x}{R_2}\right)^2 + \left(\frac{H_r}{R_1} + \frac{H_t}{R_2}\right)^2 + \left(\frac{-z}{R_1} + \frac{-z}{R_2}\right)^2}} \end{aligned} \tag{A-4}$$

We will first solve (A-4) for the limiting values of *x* by setting *z* = 0. Once we have the limiting values for *x*, we will then develop an equation that gives the cross-range values at specified values of *x* between these limits. Upon setting *z* = 0 and rearranging terms, we obtain

$$\begin{aligned} C_B &= \left\{\left[\frac{\frac{G}{R_2} - x\left(\frac{1}{R_1} + \frac{1}{R_2}\right)}{\frac{H_r}{R_1} + \frac{H_t}{R_2}}\right]^2 + 1\right\}^{-1/2}, \text{ or} \\ &\left[\frac{R_1 G - x(R_1+R_2)}{R_2 H_r + R_1 H_t}\right]^2 = \frac{1}{C_B^2} - 1 = K^2 \end{aligned} \tag{A-5}$$

Upon taking the square root and again rearranging terms, we obtain

$$R_1\left(G - x \mp KH_t\right) = R_2\left(\pm KH_r + x\right) \tag{A-6}$$

We will have to solve (A-6) using both the positive and negative values of *K* to obtain both the upper and lower limits of *x*. Now substituting for R1 and R2 in (A-6) because *x* appears in these factors, squaring both sides of (A-6) and letting $\alpha = G \mp KH_t$ and $\eta = \pm KH_s$,

$$\begin{aligned} &\left(x^2 + H_r^2\right)\left(\alpha^2 - 2\alpha x + x^2\right) = \\ &\qquad \left(G^2 - 2Gx + x^2 + H_t^2\right)\left(\eta^2 + 2\eta x + x^2\right) \end{aligned} \tag{A-7}$$

Upon multiplying the terms in (A-7) and making the following substitutions:

$$\begin{aligned} c_3 &= 2\eta - 2G + 2\alpha \\ c_2 &= \eta^2 - 4\eta G + G^2 + H_t^2 - \alpha^2 - H_r^2 \\ c_1 &= 2\eta\left(G^2 + H_t^2\right) - 2G\eta^2 + 2\alpha H_r^2 \\ c_0 &= \eta^2\left(G^2 + H_t^2\right) - \alpha^2 H_r^2 \end{aligned}$$

We can now obtain the following cubic equation for *x*:

$$c_3 x^3 + c_2 x^2 + c_1 x + c_0 = 0 \tag{A-8}$$

Although [21] provides a general method for solving a cubic equation, we have found that in the current case all the roots are real. Therefore, we have chosen to employ a method documented on the Web site

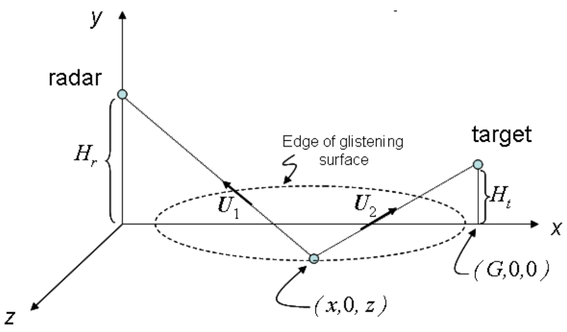

Fig. A-1: Assumed Geometry

http://mathworld.wolfram.com/CubicFormula.html. To implement this process, make the following substitutions:

$$
\begin{aligned}
a &= \frac{c_2}{c_3}, \\
b &= \frac{c_1}{c_3}, \\
c &= \frac{c_0}{c_3}, \\
Q &= \frac{b}{3} - \frac{a^2}{9}, \\
R &= \frac{ab}{6} - \frac{c}{2} - \frac{a^3}{27}, \text{and} \\
\Theta &= \cos^{-1}\left(R/\sqrt{-Q^3}\right)
\end{aligned}
$$

The following formulas then calculate the three solutions to the cubic equation:

$$
\begin{aligned}
x_1 &= 2\sqrt{-Q}\cos(\Theta/3) - a/3 \\
x_2 &= 2\sqrt{-Q}\cos(\Theta/3 + 2\pi/3) - a/3 \\
x_2 &= 2\sqrt{-Q}\cos(\Theta/3 + 4\pi/3) - a/3
\end{aligned}
\tag{A-9}
$$

Equations (A-9) provide one reasonable solution that lies between the radar and the target and two unrealistic solutions that are not between the radar and the target. Equations (A-9) must be calculated twice, once for the positive value of *K*, and once for the negative value of *K*, to obtain both the upper and lower limits on the glistening surface that lies between the radar and the target.

A. Calculation of the cross-range extent of the glistening surface

To calculate the cross-range extent of the glistening surface for specified values of *x* that lie between the *x* limits just calculated, return to (A-4) and generate a modified version of (A-5) that includes the factor *z*. This yields the following equation:

$$
\begin{aligned}
\left[\frac{R_1 G - x(R_2 + R_1)}{R_2 H_r + R_1 H_t}\right]^2 + \left[\frac{z(R_1 + R_2)}{R_2 H_r + R_1 H_t}\right]^2 \\
= \frac{1}{C_B^2} - 1 = K^2
\end{aligned}
\tag{A-10}
$$

After substituting for R_1 and R_2 and doing some tedious algebra, (A-10) becomes

$$
\begin{aligned}
(z^2 + k_1)(z^2 + k_2) + (z^2 + k_3)(z^2 + k_4) + \\
\sqrt{k_1 + z^2}\sqrt{k_3 + z^2}(2z^2 + k_5) = 0,
\end{aligned}
\tag{A-11}
$$

where the various k_i terms incorporate the specified value of *x* (between the limits found in A-9) and are given by

$$
\begin{aligned}
k_1 &= x^2 + H_r^2 \\
k_2 &= G^2 - K^2 H_t^2 - 2Gx + x^2 \\
k_3 &= (G - x)^2 + H_t^2 \\
k_4 &= x^2 - K^2 H_r^2 \\
k_5 &= -2Gx + 2x^2 - 2H_t H_r K^2
\end{aligned}
$$

Upon rearranging (A-11) and some more tedious algebra, we obtain

$$
\begin{aligned}
k_8 z^6 + \left(4k_1k_3 + k_5^2 + 4(k_1 + k_3)k_5 - 4k_7 - k_6^2\right) z^4 \\
+ \left(4k_1k_3k_5 + (k_1 + k_3)k_5^2 - 2k_6k_7\right) z^2 \\
+ \left(k_1k_3k_5^2 - k_7^2\right) = 0
\end{aligned}
\tag{A-12}
$$

where

$$
\begin{aligned}
k_6 &= k_1 + k_2 + k_3 + k_4, \\
k_7 &= k_1k_2 + k_3k_4, \ \text{and} \\
k_8 &= 4\left(k_1 + k_3 + k_5 - k_6\right)
\end{aligned}
$$

Equation (A-12) can then be rewritten in the following form

$$
w^3 + aw^2 + bw + c = 0 \tag{A-13}
$$

where $w = z^2$and after letting

$$
\begin{aligned}
a &= \left(4k_1k_3 + k_5^2 + 4(k_1 + k_3)k_5 - 4k_7 - k_6^2\right) / k_8 \\
b &= \left(4k_1k_3k_5 + (k_1 + k_3)k_5^2 - 2k_6k_7\right) / k_8 \\
c &= \left(k_1k_3k_5^2 - k_7^2\right) / k_8
\end{aligned}
$$

Proceeding as before, define the intermediate variables $Q, R,$ and θ as

$$
Q = \frac{b}{3} - \frac{a^2}{9}, \tag{A-14}
$$

$$
R = \frac{ab}{6} - \frac{c}{2} - \frac{a^3}{27}, \text{ and} \tag{A-15}
$$

$$
\Theta = \cos^{-1}\left(R/\sqrt{-Q^3}\right). \tag{A-16}
$$

Then the cubic solution for (A-14) yields

$$
w_1 = 2\sqrt{-Q}\cos(\Theta/3) - a/3 \tag{A-17}
$$

$$
w_2 = 2\sqrt{-Q}\cos(\Theta/3 + 2\pi/3) - a/3 \tag{A-18}
$$

$$
w_3 = 2\sqrt{-Q}\cos(\Theta/3 + 4\pi/3) - a/3 \tag{A-19}
$$

Upon letting $z = \sqrt{w}$,

$$z_1 = \pm\sqrt{2\sqrt{-Q}\cos\left(\Theta/3\right) - a/3}, \tag{A-20}$$

$$z_1 = \pm\sqrt{2\sqrt{-Q}\cos\left(\Theta/3 + 2\pi/3\right) - a/3}, \text{and} \tag{A-21}$$

$$z_1 = \pm\sqrt{2\sqrt{-Q}\cos\left(\Theta/3 + 4\pi/3\right) - a/3}. \tag{A-22}$$

Because the k_i terms contain only K^2, the sign chosen for K does not matter when computing z. In the numerical test cases considered so far, $w_1 > 0$, $w_2 < 0$ and $w_3 < 0$, so the only real solutions for z come from the equation for z_1.

REFERENCES

[1] I. E. Telatar and D. N. C. Tse, "Capacity and mutual information of wideband multipath fading," *IEEE Trans. on Information Theory*, vol. 46, no. 4 (July), pp. 1384–1400, 2000.

[2] R. G. Gallager, *Information Theory and Reliable Communication*. Wiley, 1968.

[3] E. A. Lee and D. G. Messerschmitt, *Digital Communications*. Kluwer Academic Publishers, 1988.

[4] M. Skolnik, *Radar Handbook*, 2nd ed. McGraw Hill, 1990.

[5] ——, *Introduction to Radar Systems*, 2nd ed. McGraw Hill, 1980.

[6] S. Blackman and R. Popoli, *Design and Analysis of Modern Tracking Systems*. Artech House, 1999.

[7] W. S. Ament, "Toward a theory of reflection by a rough surface," *Proc. IRE*, vol. 41, pp. 142–146, January 1953.

[8] P. Beckmann and A. Spizzichino, *The Scattering of Electromagnetic Waves from Rough Surfaces*. Pergamon Press, Artech House, 1987.

[9] D. Barton, *Radar System Analysis and Modeling*. Artech House, 2005.

[10] P. Hansen, K. Scheff, E. Mokole, and E. Tomas, "Dual frequency measurements of ocean forward scatter with ultrawideband radar," in *Proceedings IEEE 2001 Radar Conference*, 2001, pp. 376–381.

[11] J. Smit, J. Cilliers, C. Baker, and J. Hanekom, "X-band high range resolution radar measurements of sea surface forward scatter at low grazing angles," in *Radar Conference, 2008. RADAR '08. IEEE*, May 2008, pp. 1–4.

[12] Q. Lei and M. Rice, "Multipath channel model for over-water aeronautical telemetry," *Aerospace and Electronic Systems, IEEE Transactions on*, vol. 45, no. 2, pp. 735–742, April 2009.

[13] A. R. Miller, R. M. Brown, and E. Vegh, "New derivation for the rough-surface reflection coefficient and for the distribution of sea-wave elevations," in *IEE Proceedings*, vol. 131. Pt H, no. 2, April 1984, pp. 114–116.

[14] C. I. Beard, "Coherent and incoherent scattering of microwaves from the ocean," *IRE Transactions on Antennas and Propagation*, vol. AP-9, Sept., pp. 470–483, 1961.

[15] D. Barton, "Multipath analysis," private communication, December 2005.

[16] D. E. Kerr, *Propagation of Short Radio Waves*. McGraw-Hill, 1951.

[17] D. Barrick, "Rough surface scattering based on the specular point theory," *Antennas and Propagation, IEEE Transactions on*, vol. 16, no. 4, pp. 449–454, Jul 1968.

[18] I. Rusnak and J. Moreshet, "Specular multipath from rough correlated surfaces," in *IEEE Radar Conference*, vol. proceedings May, 1995, pp. 419–424.

[19] B. Smith, "Geometrical shadowing of a random rough surface," *Antennas and Propagation, IEEE Transactions on*, vol. 15, no. 5, pp. 668–671, Sep 1967.

[20] Y. Karasawa and T. Shiokawa, "Characteristics of L-band multipath fading due to sea surface reflection," *Antennas and Propagation, IEEE Transactions on*, vol. 32, no. 6, pp. 618–623, Jun 1984.

[21] M. Abramowitz and I. A. Stegun, Eds., *Handbook of Mathematical Functions with Formulas, Graphs, and Mathematical Tables*, 9th ed. New York: Dover, 1972.

Kent Haspert (M'00) received a B.S. in aerospace engineering (1965) and an M.S. (1967) and Ph.D. in electrical engineering (1970) from the University of Maryland, College Park. While at the Institute for Defense Analyses, he has primarily concentrated on air defense system issues. For the past 10 years, Dr. Haspert has been supporting the Joint Integrated Air and Missile Defense Organization. Much of this work has focused on radar systems and their application to air defense issues such as target detection, and tracking. He has also evaluated the use of synthetic aperture radar for finding land mines, served on an Air and Missile Defense Advisory Panel, and a panel that evaluated future tracking system concepts and implementations. Previously at IDA, he was involved in a joint-staff-sponsored investigation of air and missile defense alternatives, and flight test evaluations and associated computer system modeling of joint engagement zone concepts. Before joining IDA, he worked at ARINC Research Corporation and RJO Enterprises, where he evaluated air traffic control systems and various military command, control, communications and computer systems.

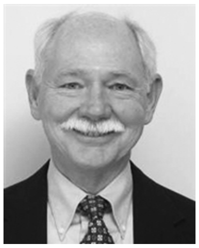

Michael Tuley (S66-M66-SM84-F97) earned a BEE from Auburn University in 1966 and an MSEE from the Georgia Institute of Technology in 1972. After five years service as a nuclear qualified, submarine officer and graduate school, he joined the Georgia Tech Research Institute where he participated in and directed radar-related programs, with a focus on Radar Cross Section prediction, Radar Cross Section Reduction, clutter, multipath and radar signal processing. Since 1998, he has been a Research Staff Member at the Institute for Defense Analyses, where he provides support to the Office of the Secretary of Defense, the Defense Agencies and the Department of Homeland Security on a wide range of sensor and surveillance programs. He is a coauthor of Radar Cross Section (SciTech 2004), and authored chapters in two additional books on Radar measurement techniques.

REPORT DOCUMENTATION PAGE

Form Approved
OMB No. 0704-0188

1. REPORT DATE May 2010	2. REPORT TYPE Final	3. DATES COVERED *(From–To)* January 2009 – December 2010

4. TITLE AND SUBTITLE

Comparison of Predicted and Measured Multipath Impulse Responses

5a. CONTRACT NUMBER
DASW01 04 C 0003

5b. GRANT NUMBER

5c. PROGRAM ELEMENT NUMBER

6. AUTHOR(S)

Kent Haspert
Michael Tuley

5d. PROJECT NUMBER

5e. TASK NUMBER
IDA CRP C2136

5f. WORK UNIT NUMBER

7. PERFORMING ORGANIZATION NAME(S) AND ADDRESS(ES)

Institute for Defense Analyses
4850 Mark Center Drive
Alexandria, VA 22311-1882

8. PERFORMING ORGANIZATION REPORT NUMBER

IDA Document NS D-3957
Log: H 10-000769

9. SPONSORING / MONITORING AGENCY NAME(S) AND ADDRESS(ES)

Institute for Defense Analyses
4850 Mark Center Drive
Alexandria, VA 22311-1882

10. SPONSOR/MONITOR'S ACRONYM(S)

11. SPONSOR/MONITOR'S REPORT NUMBER(S)

12. DISTRIBUTION/AVAILABILITY STATEMENT

Approved for public release; distribution is unlimited. (27 October 2009)

13. SUPPLEMENTARY NOTES

14. ABSTRACT

The fundamental concepts used to evaluate multipath effects date back over 50 years. Today's technology can support wide-bandwidth communications and radar systems that were not available or considered when these multipath concepts were being formulated. This paper presents a slightly modified version of the original analytical approaches for evaluating multipath effects and compares the predicted multipath to data collected from a wideband instrumentation radar. The multipath model presented herein covers both the specular (coherent) and diffuse (noncoherent) components of multipath. The test data were collected for conditions strongly favoring diffuse multipath, but the experimental technique supported detection of any unanticipated specular contributions. Because the purpose of this validation effort was to perform an in-depth examination of multipath effects, the demanding test conditions revealed a couple of real-world effects that had to be addressed. After incorporating these effects into the analytical multipath formulations, we were able to show very close agreement between the predicted and observed multipath.

15. SUBJECT TERMS

multipath, wide-bandwidth, specular, diffuse

16. SECURITY CLASSIFICATION OF:			17. LIMITATION OF ABSTRACT	18. NUMBER OF PAGES	19a. NAME OF RESPONSIBLE PERSON Mr. Philip Major
a. REPORT Uncl.	b. ABSTRACT Uncl.	c. THIS PAGE Uncl.	SAR	11	19b. TELEPHONE NUMBER *(include area code)* 703-845-2569

Standard Form 298 (Rev. 8-98)
Prescribed by ANSI Std. Z39.18

This publication is approved for public release and has been accepted by IEEE for publication in a forthcoming issue of *IEEE Transactions on Aerospace and Electronic Systems*.